CRYSTAL GROWTH & DESIGN

pubs.acs.org/crystal

Article

Electrochemically Assisted Growth of Hopper and Tabular Calcite under Confinement

Joanna Dziadkowiec,* Gaute Linga, Lukas Kalchgruber, Sunil Kavunga, Hsiu-Wei Cheng, Ola Nilsen, Coen Campsteijn, Boaz Pokroy, and Markus Valtiner

Cite This: https://doi.org/10.1021/acs.cgd.3c01433

Read Online

ACCESS | Metrics & More | Article Recommendations | Supporting Information

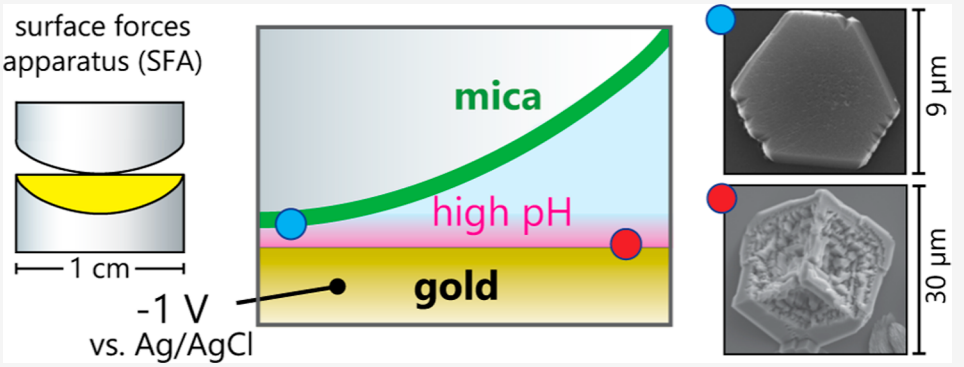

ABSTRACT: Crystallization under confinement is commonplace in nature and offers new pathways to engineer crystals with the desired morphologies in a controlled and reproducible manner. In this work, we demonstrate the electrochemically assisted, in situ formation of hopper and tabular calcite crystals within a wedge-like pore formed by confinement induced by the surface force apparatus (SFA). In this geometry, the distance between the confining surfaces decreases continuously from hundreds of micrometers to a few nanometers in a single experimental setup. Calcium carbonate precipitation followed in real-time is triggered by elevating the pH and thus supersaturation directly inside the pore. The pH increase is tracked with a fluorophore tracer and calculated analytically. The unusual calcite crystal habits are obtained in the absence of precipitation-modifying additives and vary as a function of the distance between the confining walls, where at the largest surface separations, hopper crystals form on the gold surface, whereas flat, tabular calcite forms on mica when the confining distance was below 5 μm. Hexagonal or triangular calcite plates exhibit surfaces dominantly defined by rough (001) planes and increase in their surface area-to-volume ratios with decreasing SFA pore thickness. Stabilization of calcite plates bound by (001) faces is a cooperative effect of the oriented growth of calcite on the confining, negatively charged mica walls and the confinement shape, which promotes the development of calcite morphology in the rapid crystal growth directions. The heterogeneous crystallization of calcite is preceded by the nucleation and spreading of a front composed of submicrometer-sized calcium carbonate particles visualized in situ in the SFA pore. Our work demonstrates abundant crystal growth under nanoscale confinement facilitated by elevated pH and a high surface charge of the confining walls.

INTRODUCTION

Crystallization in nature frequently involves nucleation and growth in solution-filled pores and cavities under varying degrees of spatial confinement. The availability of reagents in a given pore geometry, often limited by diffusion-dominated transport in submicrometer pores, and the physicochemical properties of confining surfaces are decisive factors that determine the outcome of crystallization in pores.[1−3] A common challenge is to synthesize nanometer-thin but elongated and platy crystals as such shapes are often expressed in biominerals[4,5] but are difficult to achieve in conventional bulk-solution precipitation methods.

Calcium carbonate comprises three crystalline polymorphs: vaterite, aragonite, and calcite, and it is a widespread compound in natural environments[6] and industry.[7] The elaborate morphologies and remarkable properties of calcium carbonate biominerals, which precipitate within semi-isolated compartments,[8] have inspired multiple studies on $CaCO_3$ growth under spatial confinement. Limited volumes often reduce nucleation rates and affect the kinetics of amorphous-to-crystalline phase transformations, which commonly results in the prolonged existence of metastable amorphous calcium

Received: December 1, 2023
Revised: March 5, 2024
Accepted: March 6, 2024

carbonate (ACC) phases within pores, with respect to the bulk. ACC stabilization has been observed across multiple scales from nanometer-sized cavities[9,10] to micrometer-thick pores.[11−18] A subsequent transformation of ACC to a crystalline phase within constrained spaces, common to biomineral-forming organisms, provides a pathway to obtain single inorganic $CaCO_3$ crystals with elaborate morphologies imposed by 3D templates in the absence of organic additives.[19,20] It is, however, not entirely understood which factors dominate polymorph selectivity of metastable ACC to crystalline $CaCO_3$ transformation within pores,[21] with possible synergistic effects of precipitation solution composition and interfacial energy relationships including the presence of charged interfaces, temperature, and epitaxial substrate templating.[21−25] While the separation of hydrated ACC clusters from solution has been shown to display no significant thermodynamic barrier[26] and ACC nanoparticles can precipitate in confined solution without the energetic aid from the confining walls,[18,27] the subsequent crystallization of ACC into $CaCO_3$ often proceeds via heterogeneous nucleation.[18,21]

Heterogeneous nucleation on substrates that exhibit active nucleation centers comprises a thermodynamic pathway to reduce the nucleation barrier associated with the formation of a new surface[28] and offers control over the crystallization process via epitaxial matching.[29] For the growth of crystalline phases under confinement, with abundant solid/solution interfaces, one may expect that heterogeneous nucleation on pore walls frequently prevails and that the physicochemical properties of confining walls significantly influence the crystal growth at its various stages.[30] For example, polymorph selectivity has been attributed to subtle variations of the surface charge of the pore walls,[23] pore-size-dependent ion distribution at charged pore walls, or electrical double-layer overlap when pore sizes are in the nanometer range.[10] Electrostatic interactions between pore walls and a growing crystal can possibly stabilize dipolar surfaces that are not present on the equilibrium morphology of a mineral phase.[21,31] Structural matching or stereochemical compatibility between the confining walls and the growing crystals can be used to control nucleation density and crystal orientation within pores.[20,24,32]

Crystals with preferential orientations can also grow under confinement without the epitaxial lattice matching with pore wall substrates, where the pore shape facilitates anisotropic growth of minerals.[33] This scenario has been frequently demonstrated in nano- to micrometer elongated pores where the fast-growing crystallographic directions are coincident with the long pore axis.[33−37] Small pore volumes lead to mass transport limitations, which generate ion concentration gradients across the confined crystal face and may result in rough morphologies with rims and cavities.[38,39] A given pore shape may also promote localized nucleation and growth in specific regions of pores, driven by various phenomena such as uneven material transport in anisotropically shaped pores[40] and thermodynamic interfacial energy effects.[31] As such, it is expected that pore geometries exist that can either speed up or slow down nucleation with respect to a flat surface of the same material.[41]

Nucleation in confined volumes is often hindered due to lower nucleation probability than in bulk, with few or no crystals growing under nanoscale confinement and with long-term stabilization of amorphous phases, as has been demonstrated in the previous works studying the growth of calcium carbonate in the surface force apparatus (SFA) by Stephens et al.[11] and Wang et al.[15] To overcome this issue, we use electrochemical reactions inside the pore to raise pH and thus supersaturate with respect to $CaCO_3$ and enhance $CaCO_3$ precipitation under confinement. Electrochemically assisted deposition of carbonates on a metal surface is driven by a local increase of pH at the cathode during the cathodic reduction of oxygen dissolved in water at a high negative applied electrochemical potential (typically below −1 V vs SHE for gold surface)[42,43] (eq 1). Hydroxide anions formed at the metal electrode/solution interface change the pH of the solution, resulting in the deprotonation of bicarbonate to form carbonate. As the solubility of calcium carbonates decreases with increasing pH, this means that the supersaturation of the solution increases leading to heterogeneous precipitation of $CaCO_3$ (eqs 2 and 3).[42,44]

$$O_2 + 2H_2O + 4e^- \rightleftharpoons 4OH^- \quad (1)$$

$$HCO_3^- + OH^- \rightleftharpoons CO_3^{2-} + H_2O \quad (2)$$

$$Ca^{2+} + CO_3^{2-} \rightleftharpoons CaCO_3(s) \quad (3)$$

At higher negative potentials, the hydrogen evolution reaction may occur[43]

$$2H_2O + 2e^- \rightleftharpoons H_2 + 2OH^- \quad (4)$$

We employ this electrochemical scaling process to induce precipitation of $CaCO_3$ under confinement formed in electrochemical SFA (EC-SFA).[45] In EC-SFA, an elongated open pore with surface separations varying continuously from a few nanometers to hundreds of micrometers is formed by mica surface pressed against the gold electrode. Using this versatile setup for studies of crystal growth,[11,15,46−48] we aim to study precipitation as a function of a well-defined and varying confinement distance in a single experiment. Precipitation is monitored in situ both in the SFA-attached camera and via interferometric fringes owing to the inclusion of multiple-beam interferometry (MBI). Our work identifies preferential sites for crystal growth and demonstrates a continuous change of calcite crystal habit with varying pore thickness.

MATERIALS AND METHODS

Preparation of Surfaces. We primarily used mica and gold surfaces in the electrochemically assisted precipitation experiments. Mica surfaces used as top confining walls were prepared following the standard SFA methodology.[49] Atomically smooth, optical-grade muscovite mica (Ruby Mica, V-1/V-2, S&J Trading Inc.) was freshly cleaved to a uniform thickness of 1−10 μm and cut with surgical scissors. The pieces of mica were back-coated with 45 nm of Au using an in-house-built thermal evaporator to facilitate the collection of interferometric signal and glued to standard fused-quartz half-cylindrical SFA disks (SurForce LLC) with EPON 1004F glue. Smooth gold Au(111)[50] surfaces, used as a bottom confining surface and working electrodes (WEs), were prepared by mica-template stripping. A 45 nm thick gold (99.99% purity, Ted Pella, Inc.) layer was deposited on a freshly cleaved thin mica sheet using an in-house-built thermal evaporator. The gold-coated sheets were cut with scissors and glued (gold side facing the glue) to SFA disks with hot melt EPON 1004F resin. Once cooled, the mica could be removed with tweezers in air, leaving a smooth Au layer on the SFA discs. 75 nm thick aluminum oxide surfaces used in control experiments were grown on a freshly cleaved mica surface by atomic layer deposition (ALD) in a home-built flow-type reactor equipped with inert gas valves and N_2 5.0 (Nippon) as carrier gas. Base pressure was maintained at 2 mbar. We used 592 cycles of alternate pulsing of

https://doi.org/10.1021/acs.cgd.3c01433
Cryst. Growth Des. XXXX, XXX, XXX−XXX

TMA (trimethyl aluminum) and H_2O at 200 °C, with the precursor delivered from an external container kept at room temperature. Mica was coated with 45 nm of gold on the other side prior to Al_2O_3 deposition.

Electrochemically Induced Precipitation under Confinement. Electrochemically induced precipitation of $CaCO_3$ under confinement was performed by using an in-house modified SFA, coupled with MBI. The design of the SFA is described in detail by Wieser et al., 2021.[51] We used fluid cell volumes of 10 or 20 mL. The MBI fringes of equal chromatic order (FECO) were collected in an Andor imaging spectrometer equipped with an Andor Zyla camera. The in situ surface monitoring with a resolution of 0.64 nm/px was obtained by splitting a part of the light beam (with a 50:50 beamsplitter) to Quantalux TM 2.1 MP camera. We also performed a few experiments using SFA2000[52] with the equipment details as in reference,[53] in which the fluid cell has a volume of 150 mL.

In SFA, two surfaces with a semicylindrical curvature (with a radius of curvature, ROC of 2 cm) are mounted against each other, with the central axes of two cylinders crossed at 90° to yield a spherical contact area. When the surfaces are placed in contact, a single-pore geometry is formed, in which the pore height varies continuously from a few nanometers in the most confined region (extending over approximately 100 nm) to 25 μm, 1 mm away from the contact region (Figure S2). The applied load in SFA was not controlled but monitored throughout the experiments with a strain gauge force sensor and was typically below 2 N m^{-1} (normalized by the ROC).

SFA was further modified to facilitate electrochemically induced $CaCO_3$ precipitation as described by Valtiner et al., 2012.[45] The three-electrode electrochemical SFA attachment consisted of a high-purity (99.99%) gold wire (⌀ = 25 mm) WE, a high-purity (99.99%) platinum wire (⌀ = 25 mm) counter electrode (CE), and a commercial reference mini electrode RE-1S Ag/AgCl (3 M NaCl) supplied by BioLogic. The gold wire was attached to the gold surface with a small plastic clamp and a screw. The CE, which supplied the current to the gold WE, was placed around the two SFA surfaces. The electrochemical potential was applied to the WE using Gamry Interface 1000 potentiostat, with respect to the reference electrode (RE). $CaCO_3$ precipitation was initiated by supplying a high negative potential between −1 and −1.2 V vs Ag/AgCl. In a typical experiment, we continuously apply this negative potential for approximately 1−3 h until the precipitation stops, as observed in the SFA-attached camera. Once the negative potential is switched on, $CaCO_3$ crystals instantaneously grow on the surfaces. Control measurements were performed with no potential applied and showed only scarce precipitation on the surfaces, with the growth happening within 30 min after the solution injection.

All $CaCO_3$ primary precipitation experiments were performed in undersaturated salt solutions prepared by mixing 50 mM $CaCl_2{\cdot}2H_2O$ (≥99.0%) and 25 mM $NaHCO_3$ (≥99.5%) Sigma-Aldrich, ReagentPlus salts in 1:1 volumetric ratio. The solutions were freshly prepared by using Milli-Q water (IS = 10^{-5} M) and freshly mixed directly before each experiment. The mixed salt solution was injected into the SFA liquid chamber (volume ∼20 mL) using 0.2 μm poly(ether sulfone) (PES) syringe filters. During the injection, the mica and gold surfaces were kept in contact. Mica surfaces are scarcely soluble, and the release of ions from mica does not significantly modify the composition of solutions used in this study (e.g., K^+ release from mica at pH 8 within 24 h is 0.2 mM[54]).

We also performed several types of control $CaCO_3$ precipitation experiments: on an isolated gold surface; with mica and gold surfaces placed far away from each other (∼1.2 to 1.8 μm at the point of closest approach); at higher supersaturation using 50 mM $CaCl_2{\cdot}2H_2O$ and 25 mM $NaHCO_3$; at higher ionic strength in the presence of NaCl; with added Mg^{2+}; in gold−gold configuration with one Au surface acting as WE and the second Au surface as a confining wall with no potential applied; and with Al_2O_3-coated mica against gold WE. We also performed a set of experiments in the presence of Ar. Ar gas purging was used to limit the dissolved oxygen content in the calcite precipitation solution. For that, the tubing connected to the Ar gas reservoir was placed directly in solution within the SFA liquid cell. Ar was then continuously purged at a low pressure to avoid intensive gas bubbling. The summary of all experiments is shown in Figure S1.

Postexperimental Characterization. The crystal heights on mica were measured with a NanoFocus optical profilometer equipped with a confocal μsurf probe. Crystal habits and spatial locations were observed with a scanning electron microscope using FEI Quanta 250 FEG SEM or Hitachi SU5000 FE-SEM. The samples for scanning electron microscopy (SEM) observations were coated with a few nanometer-thick gold or carbon layers. $CaCO_3$ phase identification was based on morphological characterization with SEM. Crystal topography was performed with a JPK NanoWizard 4 BioScience atomic force microscope in air using the quantitative imaging (QI) mode with a ContAl-G cantilever (NanoSensors, k = 0.2 N m^{-1} and l = 450 μm).

Modeling of Applied Potential Distribution and Analytical Calculations of pH. We used COMSOL Multiphysics version 5.6. software to simulate the distribution of the applied electric potential within the SFA setup. The details of Comsol modeling are described in Supporting Information, Figure S3. Analytical calculations of solution pH near the gold surface as a function of time and distance from the unconfined gold electrode in water and in calcite precipitation solution are described in detail in Supporting Information, Section S1.

Monitoring of Solution pH. The pH evolution in the solution contacting the gold WE after the application of negative potential (−1 V vs Ag/AgCl) was visualized in an unconfined system with pH-responsive dye phenolphthalein (at 1 mM concentration), which becomes pink above pH 8.3.[55] Qualitative fluorescence measurements were used to follow the pH changes in the solution confined between two SFA surfaces. For that, we built a small fluid cell mimicking our SFA geometry. The cell consisted of a 2 cm high plexiglass ring with two glass slides attached to the top and the bottom of the ring with a two-component, self-curing silicone rubber (Reprorubber). The top glass slide had a thin (∼10 μm), 2 × 2 cm^2 freshly cleaved mica glued to it with the hot melt EPON1004 glue. A spherical SFA glass disc (with a radius of curvature of 2 cm), coated first with a thin layer of UV-cured soft epoxy Norland NOA 65 and then with 50 nm of Au in a thermal evaporator, was used as the WE. Thus, we used a "sphere-on-flat" contact geometry, where a spherical SFA disc presses on a flat surface, equivalent to two SFA cylindrical discs crossed at 90°. The gold disc was fixed to the bottom glass slide with a thin, soft, and hollow tubing spacer between the disc and the glass slide to provide some elasticity upon pressing the top mica-glass surface onto the gold disc. The resultant spherical contact area had a radius of approximately 500 μm. Gold and platinum wires (CE) and a mini reference Ag/AgCl electrode were connected as in the SFA measurements through the openings made in the plexiglass ring and sealed with parafilm. A syringe-injection port was added to allow for solution exchange during experiments. We performed measurements both in deionized Milli-Q water and during calcite precipitation (freshly mixed solutions of 50 mM $CaCl_2$ and 25 mM $NaHCO_3$ at a 1:1 volume ratio). We used the fluorescent pH indicator BCECF acid [2′,7′-bis(2-carboxyethyl)-5-(and-6)-carboxyfluorescein], mixed isomers, supplied by Thermofisher, sensitive to changes in pH between 6.2 and 9.5. Water-based BCECF solutions at a concentration of ∼3.5 × 10^{-8} M were prepared 1 day before the measurements. Fluorescence microscopy was performed on a Dragonfly 505 (Andor) spinning disc microscope (widefield mode) using a Nikon CFI Plan Fluor ELWD 20x (0.45 numerical aperture) objective. Quantitative changes in fluorescence signal were simultaneously measured by time-lapse microscopy at ex/em 445/480 nm (pH-independent signal at isosbestic point) and at ex/em 488/525 nm (pH-dependent signal) during the switch of the negative potential −1 V vs Ag/AgCl. Changes in the fluorescence intensity with time were analyzed in ImageJ software by taking the average intensity of the whole field of view of 600 × 600 μm^2. We imaged the solution in a few regions with a decreasing degree of confinement, starting from the most confined contact region and moving toward the disc edge along the X direction (Y constant). The focus (Z height) was set on the surfaces in contact and not changed while moving to lower

https://doi.org/10.1021/acs.cgd.3c01433
Cryst. Growth Des. XXXX, XXX, XXX−XXX

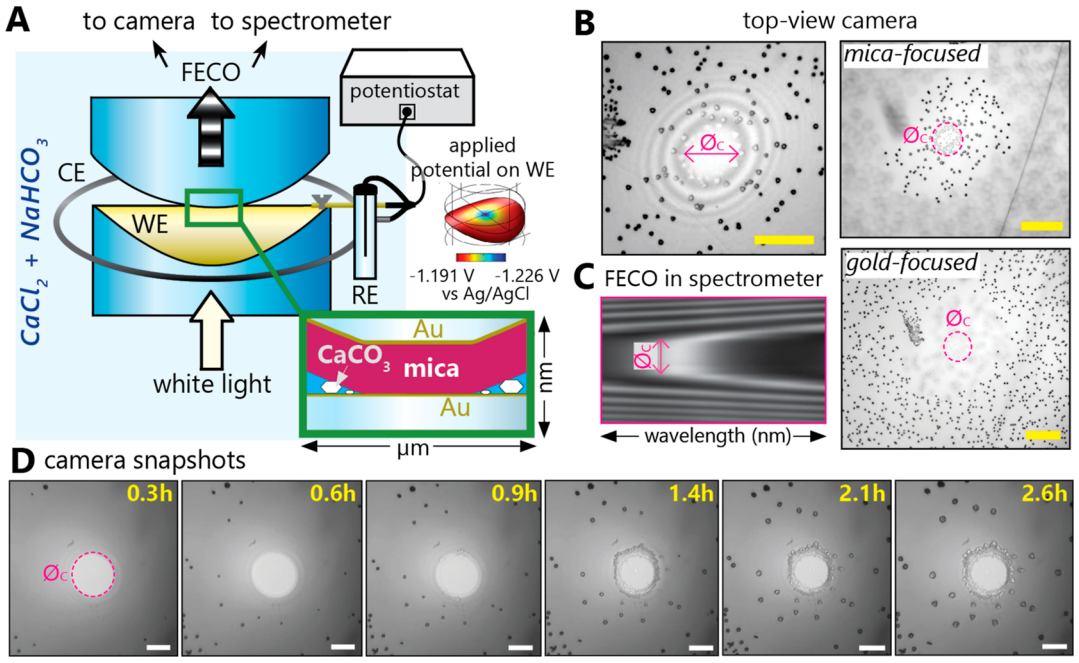

Figure 1. SFA experimental setup. (A) Calcite ($CaCO_3$) precipitation is electrochemically induced in a pore formed by two SFA cylindrical discs crossed at 90°, filled with a calcite precipitation solution ($CaCl_2$ + $NaHCO_3$). Distance between the surfaces across the contact region is measured with MBI: white light passes through the semireflective surfaces and yields FECO. The green inset shows a cross-section through the contact region with mica pressed against the gold WE. WE, a platinum wire CE, a Ag/AgCl RE, and a potentiostat comprise the electrochemical setup. The distribution of applied potential calculated in COMSOL (defined as electrolyte potential) is shown for a semiconfined WE (100 nm thick gap in the point of the disc closest approach; more details in Figure S3). (B) SFA camera top-view on surfaces at the end of precipitation in one representative experiment, with Newton rings outlining the contact region between mica and gold of diameter ϕ_C. Mica- and gold-focused panels on the right show preferential growth of $CaCO_3$ on mica around the contact region of diameter ϕ_C outlined with a dashed line. The scale bars are 100 μm. (C) Example of FECO corresponding to mica and gold surfaces in contact. (D) SFA-camera snapshots from the in situ precipitation (Supporting Information, Movie M02) where the brighter circle represents the mica-gold contact region. Scale bars are 50 μm. The elapsed time is indicated in yellow.

confinements; thus, the focal plane was close to the mica surface at all times.

RESULTS

Precipitation Setup. We performed electrochemically assisted calcite precipitation under the confinement formed in SFA by two half-cylindrical surfaces pressing on each other and crossed at 90° with respect to their long cylinder axes, which comprise a typical SFA geometry, as shown in Figure 1A. A summary of all of the SFA experiments is given in Figure S1. As our surfaces can deform and flatten under pressure, a spherical contact region with a diameter of approximately 100 μm is formed, across which the surface separation is uniform and below a few nanometers. The distance between surfaces (Figure S2) increases from several nanometers at the contact region edges to ~635 μm at the cylinder edges (assuming their perfect alignment), and it is tracked in the most confined contact region with MBI.[52]

Mica and gold comprise the two confining walls. The gold surface serves additionally as a WE in our three-electrode electrochemical SFA setup together with a platinum wire as a CE and a Ag/AgCl RE. Low negative electric potential (−1 V vs Ag/AgCl) is applied to the WE using a potentiostat. COMSOL-calculated distribution of the electric potential on the gold WE/electrolyte interface shows quite uniform potential on a semiconfined WE with a little potential drop in the disc center, as shown in Figures 1A and S3.

We expect a more pronounced potential drop toward the confined contact area for nanometer-range confinement due to increased resistivity in highly confined spaces; however, its estimation is not reliable via the finite element-based COMSOL simulations. Occasional hydrogen gas bubbling observed in some of the experiments around the contact region (Supporting Information, Movie M03) suggests that we can reach negative potentials that induce water splitting and H_2 release, which has been shown to occur at applied potentials below −1.2 V vs Ag/AgCl in a similar but unconfined electrode setup.[43]

In situ $CaCO_3$ precipitation under confinement viewed in an SFA camera can be followed in Supporting Information, Movies M01−M08 (Movies M09−M16 correspond to various control experiments; see Figure S1). Figure 1B shows snapshots from a top-view SFA camera at the end of a representative electrochemically induced calcite precipitation experiment. Calcite crystals grew everywhere on the surfaces, apart from the most confined contact region. The mica-focused image reveals ring-shaped precipitation only within the confined zone around the contact, while at higher surface separations, the majority of crystals grow on the gold surface. The confining mica and gold surfaces do not fully separate from the contact during precipitation as tracked with interferometric FECO depicted in Figure 1C, in which the flattened part of the fringe corresponds to the smallest surface separation across the contact area. The change in surface separation is generally limited to a few nanometers in the center of the contact region and may be larger at the contact edges (<100 nm), which suggests that precipitates growing around the contact region can sometimes partially open the

https://doi.org/10.1021/acs.cgd.3c01433
Cryst. Growth Des. XXXX, XXX, XXX−XXX

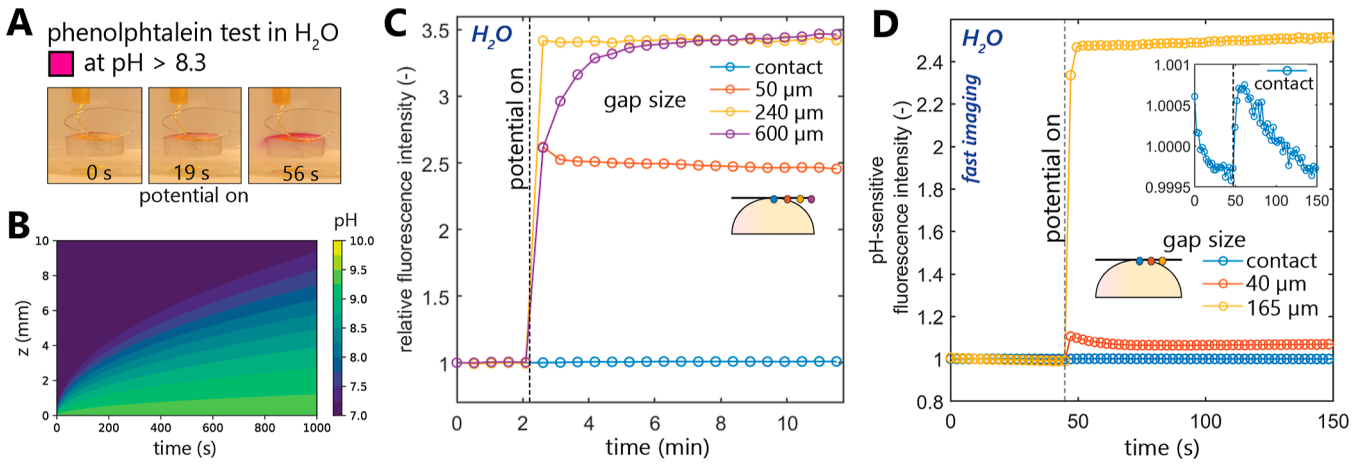

Figure 2. Evolution of pH upon the application of negative electrical potential (−1 V vs Ag/AgCl) in deionized Milli-Q water. (A) The phenolphthalein test indicated an instantaneous pH change to basic (higher than 8.3) on an unconfined gold WE surface upon the application of the electrical potential. (B) Computation of pH as a function of time and distance (z) from an isolated gold surface during the oxygen reduction reaction in water; see details (model 1) in the Supporting Information. (C) pH-dependent fluorescence signal in deionized water confined between mica and gold surfaces, measured at various confined gap sizes, as marked on a sketch. The inset shows a zoomed-in contact position (nanometer-thin gap). Fluorescence is expressed relative to pH-insensitive fluorescence signal and normalized with respect to the first measured point. Raw data are shown in Figure S5. (D) pH change upon the application of negative potential resolved in fast measurements at various degrees of confinement. Only the pH-sensitive fluorescence signal was measured to decrease acquisition time. The initial fluorescence intensity was normalized by the mean intensity of the signal measured within the first 20 s.

contact at its edges against the applied load, which is below 2 N m^{-1} (load normalized by the SFA disc's radius of curvature; Figure S4). Snapshots in Figure 1D show the evolution of precipitates around the mica−gold contact region with the elapsed time.

Calcite precipitation under confinement is induced by an instantaneous local increase in OH^- concentration in the vicinity of the gold WE and thus a local increase in the supersaturation with respect to calcite upon the application of a negative electrical potential (−1 V vs Ag/AgCl). A phenolphthalein test with snapshots presented in Figure 2A for an unconfined gold cylindrical disc in deionized water shows a local uniform change of solution color to pink on the whole gold WE surface once the negative potential is applied (Supporting Information, Movie M17), which corresponds to basic pH > 8.3.[55] Analytical calculations of pH change with time close to the unconfined gold surface in water indicate that pH increases to 9.4 within seconds, as depicted in Figure 2B; see details in Supporting Information, Section S1, model 1. We also explored the pH change in water confined between mica and gold surfaces. Figure 2C,D shows time-resolved qualitative pH change probed under confinement using fluorescence microscopy. For these experiments, we prepared a ∼ 10 mL volume replica of our SFA electrochemical liquid cell with a gold-coated sphere pressing on a flat mica surface and measured the fluorescence intensity of a pH-sensitive dye as a function of confinement close to the mica surface (as marked on cartoons in panels C and D). The pH change to higher values indicated by a sharp increase in relative fluorescence occurred within seconds for all probed surface separations apart from the largest 600 μm gap with a slower pH change within minutes, as shown in Figure 2C. This delay corresponds to the diffusion time required for OH^- species produced at the gold WE surface to reach the mica surface. Measurements repeated with a higher sampling frequency shown in Figure 2D confirm that a pH increase occurs within seconds for gaps below 165 μm.

We performed similar experiments in a calcite precipitation solution ($CaCl_2$ + $NaHCO_3$). The phenolphthalein test on an unconfined gold sample revealed no change of solution color to pink, indicating a pH below 8.3 (Figure S6A). This is in line with the buffering effect of HCO_3^- anions, which are converted to CO_3^{2-} at high pH (see eq 2) and with the incorporation of carbonate anions into the growing calcium carbonate precipitates, which also results in a pH decrease.[56,57] There was also no large increase in pH-sensitive fluorescence intensity in experiments performed under confinement (Figure S6B,C). These data show preferential dye incorporation into growing crystals associated with a strong local increase in the fluorescence intensity in regions with crystals and a drop in the fluorescence intensity of the confined solution (Figure S6D). Despite that, we could observe a very small increase in relative fluorescence, which was correlated with the negative potential switch, especially for a 35 μm thick gap. We interpret this change as a minor increase of the solution pH upon the application of a negative potential (1.05-fold compared to a 3.5-fold increase measured in water in a similarly sized gap). The pH measured in bulk solution was 7.7−7.8 and is in agreement with pH 7.7 calculated with PhreeqC[58] software. Based on these data, we infer that the pH close to the gold surface in the calcite precipitation solution has a value between 7.7 and 8.3. We also calculated pH change in the calcite precipitation solution during oxygen reduction on unconfined gold analytically and obtained maximum pH in the boundary layer near the gold surface of ∼7.9 (Figure S6E; see computation details in Supporting Information, Section S1, model 2). This pH value yields supersaturation with respect to calcite ($\sigma_{calcite}$) of 1.95 and supersaturation with respect to anhydrous ACC (σ_{ACC}) of 0.47 as calculated with PhreeqC based on the thermodynamic ACC data adapted from Rodriguez-Navarro et al.[59] $CaCO_3$ precipitation typically stops after 2 h, as observed in the center region of the discs, which is likely related to oxygen and ion depletion in the confined solution and the associated drop in the super-

https://doi.org/10.1021/acs.cgd.3c01433
Cryst. Growth Des. XXXX, XXX, XXX−XXX

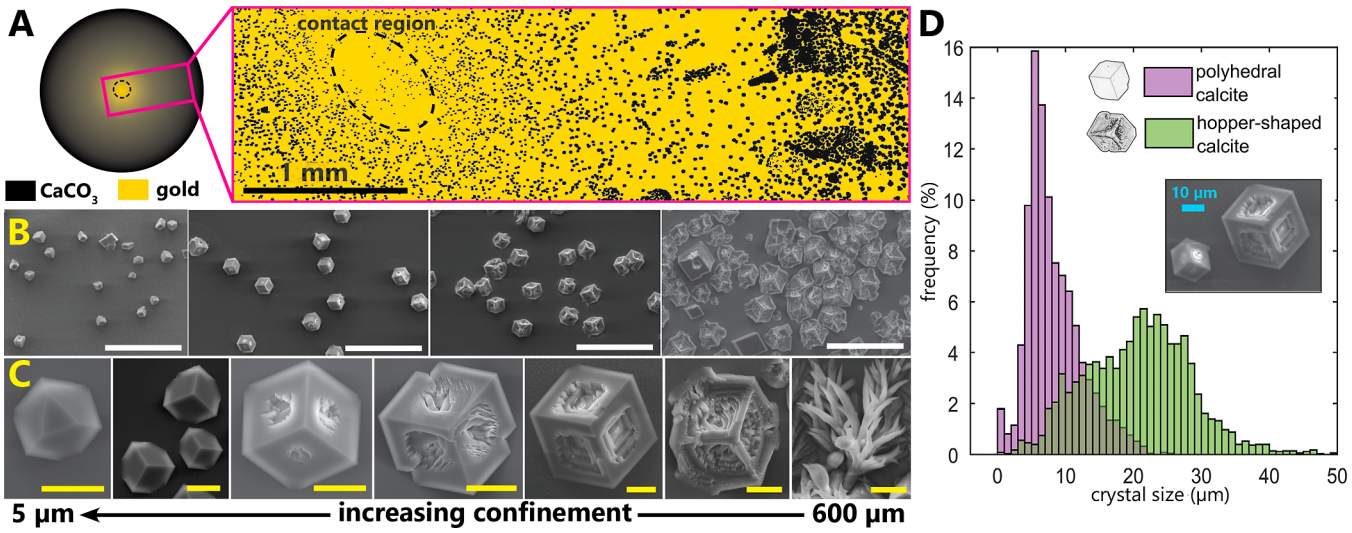

Figure 3. $CaCO_3$ precipitation on gold WE surface at the end of experiments; white scale bars are 100 μm and yellow 10 μm. (A) SFA camera image of the $CaCO_3$ crystal distribution with little precipitation around the mica−gold contact region; contact outlined with a dashed line. (B) Ex situ SEM images of $CaCO_3$ crystal sizes and density as a function of a varying confinement degree from the SFA disc center to the disc edge. (C) Zoomed SEM images showing representative $CaCO_3$ crystal habits as a function of confinement. (D) Occurrence of regular $CaCO_3$ crystals with smooth {104} faces and with hopper-shaped habits as a function of crystal size, quantified from SEM images with ImageJ software. The SEM inset image shows different degrees of hopper morphology development for smaller and larger $CaCO_3$ crystals.

saturation. A typical concentration of dissolved oxygen in water is 2×10^{-5} mol L^{-1}.

Precipitation on Gold. As evidenced by SEM and presented in Figure 3, rhombohedral calcite crystals bound by {104} faces grow abundantly on the gold WE, except from a spherical 1 mm wide region in the center of the gold surface, which comprised a contact region with mica. Within this region, where surface separations are below 5 μm, there is scarcely any precipitation on gold (Figures 3A and S7) as it preferentially occurs on the opposing mica surface (Figure 1B). Almost all calcite crystals are oriented with the (001) plane parallel to the gold surface. Both the density and size of calcite crystals are usually the highest on the disc edges and decrease toward the disc center (Figure 3B). We occasionally detect flower-like, lens-shaped, and hexagonal-shaped aggregates of vaterite platelets on gold surfaces, usually close to gold disc edges. The majority of large calcite crystals grown on the gold surface display hopper-type morphology with well-developed crystal edges and hollow crystal faces (Figures 3C and S8). As the size of the crystals increases toward the disc edges, the incidence of hopper crystals increases with the decreasing confinement. Statistical analysis of representative SEM images shown in Figure 3D indicates that a typical cutoff crystal size at which we observe the hopper morphology is ∼12 μm in diameter. We also occasionally detected dendritic crystals of calcium carbonate on the very disc edges (Figures 3C and S8G). Calcite crystals that grow close to the mica−gold contact region display smooth {104} faces, and the ones growing in the narrowest gap are truncated at the top corner with the (001) face due to the geometrical limitations preventing the development of a full calcite rhombohedron (Figure 3C). The development of hopper morphologies is very limited in control experiments with applied potential but under no confinement, in which (001)-oriented calcite with smooth {104} faces is grown on an unconfined gold surface (Figure S9). Control experiments on unconfined gold in the absence of applied potential dominantly yield vaterite and a minor amount of calcite crystals with various orientations (Figure S10).

Precipitation on Mica. Figure 4 summarizes representative calcite precipitation on confining mica surfaces, with crystals growing preferentially around the mica−gold contact region in a ring structure. There is usually little precipitation away from the contact area (Figures 4A and S11A,B), but in some experiments, we observed a substantial amount of crystals scattered on surfaces (Figure S11C) or growing locally in patches closer to the sample edges (Figure S11D). A control experiment performed with gold and mica placed further apart (minimum surface separation in the disc center, D, of ∼1.5 to 2.0 μm) shows no typical ring pattern and only scarce precipitation on the mica surface (Supporting Information, Movie M09 and Figure S12). In primary experiments, the crystals grow within 500−700 μm wide zones, as measured from contact edges (e.g., Figures 4A and S11), in which mica−gold surface separation increases from a few nanometers close to the mica−gold contact to ∼5 μm. Calcite crystals growing in this zone display a continuous change of their crystal habit with decreasing gap thickness: from well-developed calcite rhombohedra bound by {104} faces at the largest surface separations to nanometer-thick plates exposing the (001) face (Figure 4B). The calcite rhombohedra are oriented with (001) plane parallel to the mica surface. SEM images zooming on the change of crystal habit as a function of the increasing confinement are shown in Figure 4C. A schematic representation of this transition from regular to tabular calcite is shown in Figure 4D. At the highest gap size, rhombohedral calcite crystals are truncated by the (001) plane (Figure S13). The proportion of (001) faces to {104} faces increases with increasing confinement and decreasing crystal thickness. Tabular crystals with habits dominated by (001) faces display hexagonal or triangular shapes, which are in line with the trigonal symmetry of these polar faces. Figure 4E summarizes crystal height as a function of the distance from the contact center and indicates that the crystal height is limited by the space available in the gap between gold and mica surfaces;

https://doi.org/10.1021/acs.cgd.3c01433
Cryst. Growth Des. XXXX, XXX, XXX−XXX

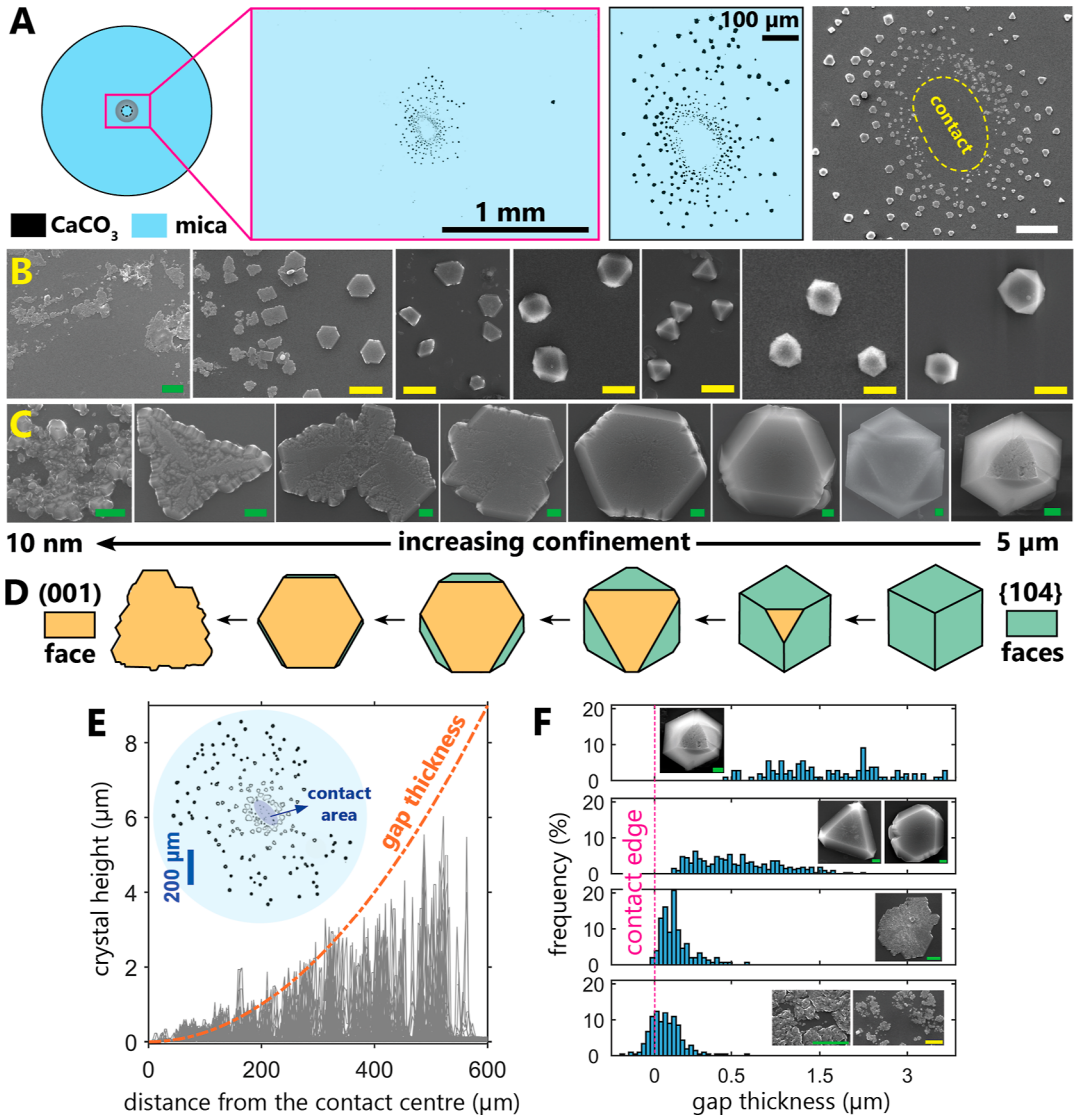

Figure 4. Calcite precipitation on the confining mica surface observed at the end of experiments; white scale bar is 50 μm, yellow 10 μm, and green 1 μm. (A) SFA camera images of the crystal distribution with crystals located dominantly around the contact region. Last panel in A is an ex situ SEM image zooming on the contact region, outlined with a dashed line. (B) Ex situ SEM images of crystal shapes as a function of a varying confinement degree from the SFA disc center to the disc edge. (C) Zoomed SEM images show a continuous change in crystal habits as a function of increasing confinement. (D) Schematic representation of crystal habit change from regular calcite bound by {104} faces growing at the largest surface separations to tabular, nanometer-thick crystals with rough pseudo (001) faces growing within the most confined region visualized with SHAPE software. (E) Crystal heights as a function of distance from the contact center were measured with an optical profilometer. The SFA gap thickness is marked with an orange line. The blue inset shows the spatial distribution of calcite around the contact area. Data from one experiment and (F) crystal types as a function of gap thickness between the confining surfaces, quantified from SEM images. Data from multiple experiments.

thus, the crystals grow to fill the available space. As such, the gap height determines the resultant type of crystal shape from truncated rhombohedral crystals to increasingly irregular aggregates, as shown in Figure 4F.

A close inspection of the morphology of the platy crystals with atomic fluorescence microscopy (AFM) and SEM reveals that the exposed (001) planes are rough and are composed of aggregated nanoparticles (Figures 5, S14, and S15); thus, they comprise pseudo (001) planes. The roughness of the (001) planes shows no correlation with the calcite plate thickness (root-mean-square; an rms roughness of 4.8 ± 2.1 nm for 1 × 1 μm^2 scans and for plate thicknesses from 51 to 428 nm; Figure S14). The calcite plates have large surface areas. The nominal surface area-to-volume ratios calculated with ImageJ for the plates shown in Figure S14 assuming their smooth faces increase with the decreasing plate thickness and range from 2.6 for the thickest plate to 23.2 for the thinnest plate. In addition, these planes often display defects concentrated along the three crystallographic [010], [1−10], and [−100] directions, which are not terminated by {104} faces at the edges (Figure S16). Precipitates growing in the smallest gap near the contact area display no regular hexagonal or triangular shape but are aggregates of irregular nanoparticles (Figures S17 and S18). Plates composed of aggregated particles that displayed crystalline {104} faces were detected in only one experiment (Figure S15A).

We also performed several control experiments. SFA tests carried out with mica replaced by a second gold surface (gold−gold surface configuration) resulted in tabular calcite crystals growing around the contact region and distributed equally

https://doi.org/10.1021/acs.cgd.3c01433
Cryst. Growth Des. XXXX, XXX, XXX−XXX

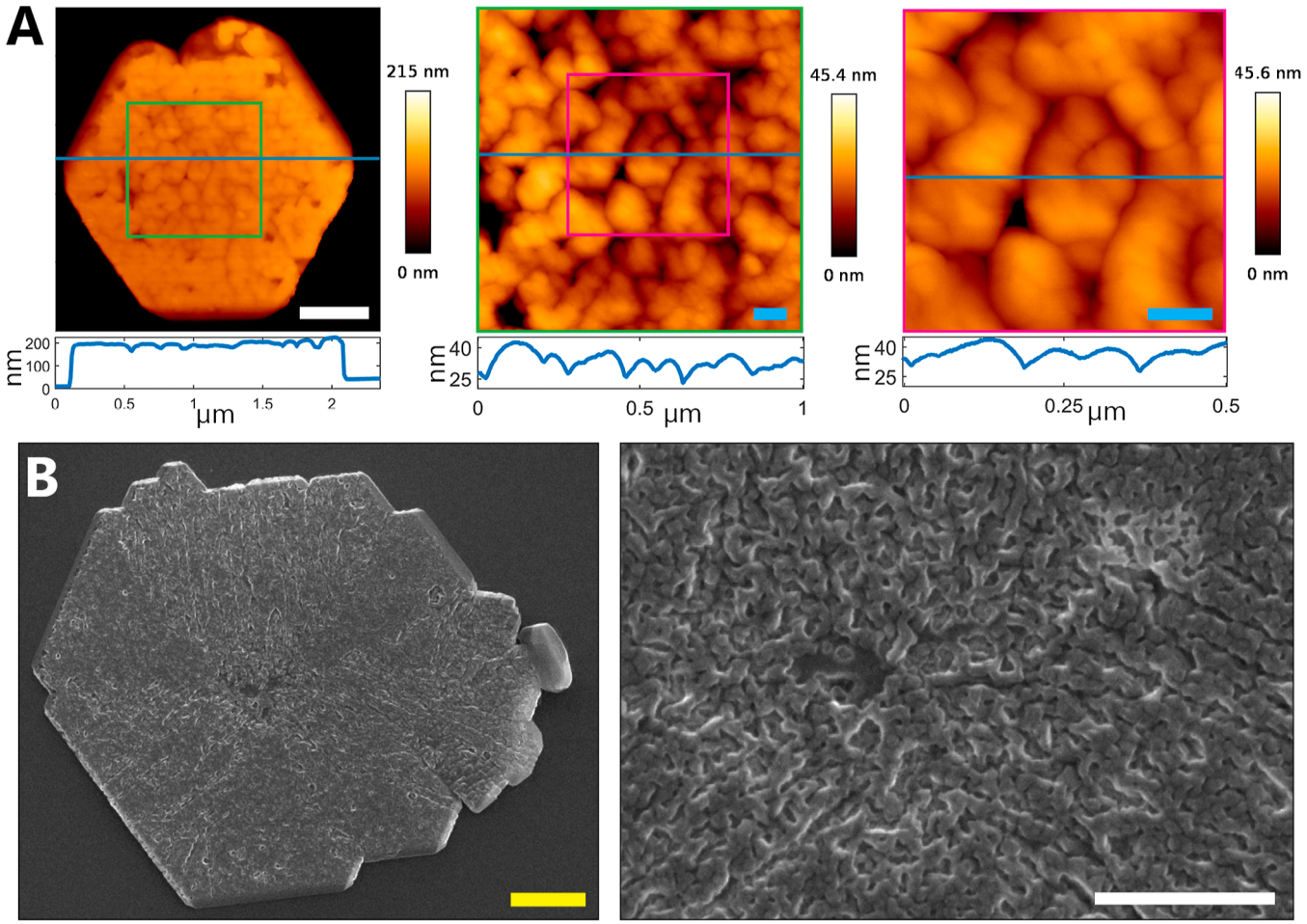

Figure 5. Rough morphology of (001) planes exposed on thin, tabular calcite; yellow scale bar is 1 μm, white 500 nm, and blue 100 nm. (A) AFM relative height maps with two zoom-ins on the rough (001) face morphology composed of aggregated nanoparticles with no distinguishable crystal faces. The plate thickness is ~200 nm. The plots show height profiles along the blue lines specified in the height maps. (B) SEM images of tabular calcite, with a zoom-in captured in the middle of the (001) plane.

densely on both gold surfaces (Figure S19). Experiments with added Mg^{2+} show a similar ring distribution of calcium carbonate precipitates on mica and precipitation on gold at higher surface separations as in primary experiments; however, the crystal habits are significantly modified with irregular shapes and smaller sizes of precipitates (Figure S20). The control experiments, in which the mica surface was coated with a thin Al_2O_3 film, show no tabular or (001)-oriented calcite crystals but instead scarce precipitation composed of vaterite and single-calcite crystals with various orientations with respect to the substrate on the Al_2O_3-coated mica and abundant calcite precipitation away from the contact on the opposing gold surface with some regions rich in vaterite (Figure S21). Experiments at higher ionic strength (E13–E14) or at higher supersaturation (E16–E17) yielded precipitates similar to those of the primary experiments (Figure S1).

Evidence for Formation of a Precursor Phase. Figure 6 presents evidence for the formation of metastable calcium carbonate precursor phase, which appears in the confined solution prior to heterogeneous calcite precipitation. In some of the SFA experiments, we could capture a slightly darker uniform front in the SFA-attached camera and observe that calcite crystals nucleate heterogeneously on surfaces only in specific areas covered by this front (Figure 6A,B; Supporting Information, Movies M03 and M06). We interpret that the darker color visible in the top-view SFA camera corresponds to a suspension, which forms in the solution confined between mica and gold surfaces. The observed drop in light intensity is therefore related to white light scattering on precursor submicron-sized precipitates. In line with the common occurrence of ACC under confinement,[1] we interpret that this precipitate is phase-separated amorphous calcium carbonate. We have observed a similar phenomenon in our previous SFA setup.[12] In our experiments, the ACC front spreads simultaneously from two directions (Supporting Information, Movie M03) or starts in a few places around the contact region (Supporting Information, Movie M06), which reflects the development of supersaturation with respect to ACC. Subsequent precipitation of calcite typically occurs after more than 10 min in a region close to the contact area, as analyzed using the white light intensity signal for crystals in one of the experiments, in which the ACC front is visible (Figure 6C). Interestingly, the light intensity in control locations with ACC but no crystals (bottom panel in Figure 6C) does not increase again once calcite precipitates, suggesting that ACC and calcite can coexist over prolonged times under confinement.

In another type of experiment, we could also induce separation of the ACC phase in small spherical domains around the contact region by purging argon gas into the

https://doi.org/10.1021/acs.cgd.3c01433
Cryst. Growth Des. XXXX, XXX, XXX−XXX

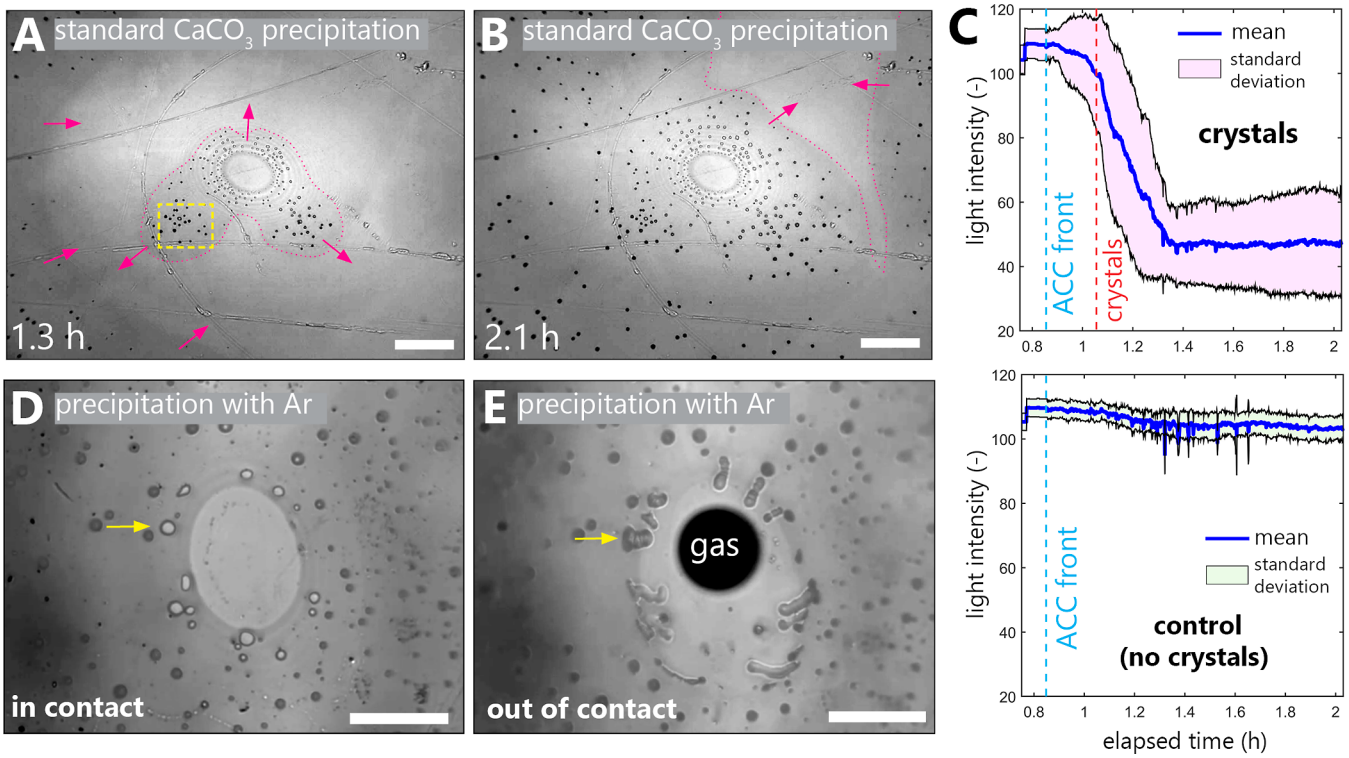

Figure 6. Precipitation of the ACC precursor phase. Scale bars are 100 μm. (A,B) Spreading of precipitation front during electrochemically induced growth of $CaCO_3$ viewed in the SFA camera. The contact region is outlined by Newton rings. Darker-colored precipitation fronts spread simultaneously from two directions: outward from the contact region and inward from the sample edges to the contact center, as marked with magenta arrows. $CaCO_3$ crystals grow on surfaces only after the front passage. Magenta dots outline the precipitation front limits. Yellow dashed line marks the analysis region used in C. Full precipitation is shown in Supporting Information, Movie M03; more snapshots are given in Figure S22. (C) Averaged white light intensity changes as a function of elapsed experimental time for (top) locations with crystals and (bottom) locations with no crystals. The appearance of the ACC front is correlated with a higher noise in the measured light intensity and a subsequent slight drop in the mean intensity. Calcite crystallization correlates with the rapid decrease in light intensity. Exact analyzed locations are listed in Figure S23. (D,E) Precipitation was characterized by argon gas purging. Bright circular features (one marked with a yellow arrow) comprise a denser liquid phase separated from the solution. These droplets deform upon mica−gold surface separation and are not a gas phase as they neither coalesce nor escape from the contact zone. Full precipitation is shown in Supporting Information, Movie M14.

precipitation solution, thus depleting the dissolved oxygen content and lowering the supersaturation with respect to calcite (Supporting Information, Movie M14). The snapshots from these experiments in Figure 6D,E show spherical patches of the ACC phase in regions where flattened calcite crystals would be usually observed in primary experiments. When we separated the surfaces from contact, the $CaCO_3$ phase behaved as droplets of a viscous gel, deforming and flowing into the contact region (Figure 6D). The fact that these droplets did not coalesce and remained on the separated surfaces indicates that they were not a gas. Ex situ SEM observations of the surfaces from these experiments showed no presence of crystals around the contact region in a typical ring-like structure in two out of three experiments. In the third experiment, we observed a partial ring with small crystals (Figure S24). These have a characteristic appearance of a small triangular or hexagonal crystal growing within a spherical region composed of smaller precipitates, reminiscent of the ACC droplets visible in Supporting Information, Movie M14.

DISCUSSION

We observed spatially varying $CaCO_3$ precipitation in an SFA wedge-like pore, with preferential crystal growth on (111) gold or (001) mica surfaces, depending on the degree of confinement. Precipitation on gold dominated for all surface separations larger than 5 μm, with prevalent growth of rhombohedral calcite crystals bound by {104} faces. The majority of large (>∼12 μm in diameter) crystals exhibited hopper-like morphologies. It has been established that interfacial instability drives the formation of such skeletal hopper crystals where crystal edges grow at higher rates than crystal faces.[60] In such a diffusion-controlled growth process, the protrusions at crystal edges can therefore experience higher supersaturation than the faces. The existence of a well-defined cutoff size (∼12 μm) above which crystals with hopper instability prevail in our SFA experiments is in agreement with the diffusion-controlled crystal growth theories by Chernov and by Mullins and Sekerka.[60−62] The occasional appearance of dendritic calcium carbonate on the very disc edges supports the formation of these precipitates due to concentration gradient-driven interfacial instability as dendrites tend to form at its highest degree.[60] The transition from equilibrium to hopper morphologies has been previously linked to very rapid crystal growth via the 2D nucleation growth mechanism possible only at very high supersaturations.[63,64] Both our control experiments on isolated gold and previous studies have shown no evidence of the extensive formation of hopper calcite in electrochemical $CaCO_3$ deposition on isolated metal surfaces,[42,43,65−68] suggesting that our confined system supports higher growth rate for calcite than has been achieved

https://doi.org/10.1021/acs.cgd.3c01433
Cryst. Growth Des. XXXX, XXX, XXX−XXX

on isolated surfaces as diffusion of OH^- out of our confined gap is limited relative to an unconfined gold surface. With OH^- diffusivity, $D = 5 \times 10^{-9}$ m^2 s^{-1} and assuming that the rate of oxygen reduction on gold is unaffected under confinement close to disc edges, the pH of the solution confined near the SFA disc edges (at a surface separation of 600 μm) can become higher relative to an unconfined gold surface at the time scale of seconds; as estimated from equation $z(t) = 2\sqrt{2Dt}$ where z is the thickness of OH^- layer and t is the time, see Section S1.1 of the Supporting Information for more details. The supersaturation with respect to calcite, $\sigma_{calcite}$, modeled for our solution in contact with the OH^--producing, unconfined gold surface reaches 1.95. Based on the simple calculations above, $\sigma_{calcite}$ in a confined solution quickly becomes higher than that in a bulk solution. This is in line with the abundant formation of hopper crystals under confinement and very few crystals with hopper morphologies detected on an isolated gold surface.

Precipitation of calcite on mica is favored at small surface separations, below ~10 μm, and this preferential growth on mica could be likely linked to better epitaxial matching of (001) calcite on mica than on gold. Both (001) mica and (111) gold surfaces have been shown to promote the oriented growth of (001)-oriented rhombohedral calcite. Epitaxy of calcite has been detected on weathered mica, with K_2CO_3 nanocrystallites facilitating oriented calcite growth,[69] or on freshly cleaved mica at higher supersaturations.[70,71] Negatively polarized Au(111) films deposited onto mica have been shown to promote oriented growth of calcite with (001) planes parallel to the substrate,[68] while polycrystalline gold or Au(111) evaporated onto silicon substrates yielded vaterite and calcite with random orientations.[29,68] In our electrochemical SFA setup, both freshly cleaved mica and mica-template-stripped (111) polarized Au films support the formation of oriented calcite crystals with (001) planes parallel to these two substrates. Both the pseudohexagonal lattice of muscovite mica (001) and the hexagonal lattice of Au(111) could provide a good epitaxial match for calcite (001), which also displays a hexagonal symmetry. The distance between adjacent Ca^{2+} within the (001) plane is 4.991 Å,[72] and the spacing between neighboring K^+ in the (001) plane of mica is 5.2 Å.[73] Au(111) has a lattice constant of 2.88 Å along the [1−10] direction; however, the distance between Au atoms in the [11−2] direction is 4.98 Å.[74] These simplified considerations indicate that gold can provide the smallest structural mismatch for Ca^{2+} in calcite, with the most similar cation spacing (see the schematic matching of lattices in 2D in Figure S25), provided that the lattice spacing of Au(111) is not affected by possible surface reconstruction triggered by the polarization of the gold electrode at high negative potentials.[75] As such, if the epitaxy governed oriented growth on mica and gold surfaces, the better epitaxial match would favor the formation of calcite on gold, assuming the same solution supersaturation conditions for both surfaces. Our control experiments on nonpolarized Au(111), in which vaterite is the dominant precipitated phase, indicate, however, that this possible epitaxy alone is not the decisive factor for the oriented growth of calcite on gold. We also did not observe any preferred orientation of calcite crystals on our Al_2O_3 films, indicating that aluminum oxide deposited on mica by ALD does not support the epitaxy or oriented growth of calcite.

Another possible cause of the growth of calcite on mica instead of gold under the largest confinement is the variation in surface charge density of gold and mica, which causes differences in ion adsorption onto the surfaces.[69] In our experiments, both mica and the polarized surface of gold are negatively charged. The structural lattice charge of mica due to isomorphic aluminum to silicon substitution is −0.34 C m^{-2}.[76] The surface charge of Au(111) at high applied potentials in our electrolyte is much lower than −0.2 C m^{-2}.[77] The (001) face of calcite is dipolar because this surface termination reflects layers of either Ca ions or CO_3 groups in the calcite crystal structure.[78] We, therefore, expect that the layer of Ca^{2+} ions is the first to assemble on negatively charged gold or mica surfaces during crystallization and that this adsorption drives oriented growth of calcite, which is supported by the lack of oriented calcite on nonpolarized gold. It has been theoretically discussed by Katsman et al.[21] that a negative charge of confining walls is sufficient to induce oriented growth of crystals due to electrostatic interactions with polar mineral faces. Growth on mica is preferential only at the smallest surface separations below 5 μm. We interpret this as a crossover separation distance below which the mica surface is in a high-pH zone and experiences a similar supersaturation with respect to calcite as gold. Within this high-pH region, calcite precipitation is preferential on mica because of its more favorable surface charge properties, in comparison with gold. Experiments in gold−gold surface configuration show that flattened (001) calcite was distributed around the contact region with equal density on both gold surfaces (as gold surfaces are in contact, there is a charge transfer between them, and they likely have a similar surface charge), which additionally points to more favorable calcite−mica interfacial energy. The surface charge of ALD-deposited Al_2O_3 films is generally low at moderately basic pH, with some works reporting the point of zero charge between pH 7 and 8.[79,80] The low surface charge might be one possible reason for the scarce precipitation of calcite on the alumina surfaces, while the presence of a substantial amount of vaterite that we detect (Figure S20D) is in agreement with the possible preferential growth of this polymorph on positively charged surfaces.[21,79] This is also in line with the precipitation of vaterite on a nonpolarized gold surface in our control experiments (Figure S10).

Calcite crystals growing on mica continuously change their crystal habit from typical rhombohedra bounded by {104} planes to flat tabular plates exposing the (001) face. As the (001) plane of calcite is dipolar, composed of a sublayer of Ca or CO_3, it is usually unstable in the absence of adsorbed species such as Li^+ ions[81,82] or organic additives.[83] In our experiments, calcite crystals can express (001) planes due to the combined effect of the oriented growth on mica and the spatial confinement of SFA. The negative charge of mica surfaces, possibly together with quite favorable lattice matching, induces the orientation of polar (001) planes parallel to the mica surface, while the shape of the SFA pore limits the growth of calcite in the constrained [001] direction. As such, the crystals are forced to grow in all the other planar directions to consume the local supersaturation and are not able to push the confining surfaces apart significantly enough to attain their equilibrium rhombohedral shape (we used applied loads below 2 N m^{-1}), which explains the increasing proportion of (001) faces to {104} planes with the increasing confinement. At the smallest surface separations, the shape of tabular calcite becomes more irregular, and the plates lose their hexagonal shapes (Figure S14), which corresponds to the

https://doi.org/10.1021/acs.cgd.3c01433
Cryst. Growth Des. XXXX, XXX, XXX−XXX

increasing importance of the directions of rapid growth in shaping the final crystal morphologies. To accommodate the flat shape, calcite plates consistently display more defects along three crystallographic directions [010], [1−10], and [−100], which are those not terminated by {104} faces. Nontypical morphologies of crystals growing under confinement, especially elongated crystals in cylindrical pores, have been frequently observed when the fast growth axes are coincident with available space for growth within a given pore.[33−37] As smooth, highly polar (001) calcite planes would be unstable in our system with no additives, they exhibit high surface roughness and are externally composed of irregular nanoparticles (Figure 5). In larger rhombohedral calcite crystals truncated with the (001) plane at the top corner, the surface roughness of (001) planes is still high but the asperities are clearly terminated by regular {104} faces. Thus, expressing this face in our system requires a high degree of surface reconstruction. Our SFA results demonstrate that the combined effect of oriented growth on the confining walls and the nanoscale spatial confinement can provide a pathway to engineer crystals with nontypical morphologies in the absence of additives. The rough (001) faces of calcite synthesized here in this fashion display exceptionally high surface area-to-volume ratios [over 20 assuming that (001) faces are smooth; rms roughness of these plates is several nanometers, as shown in Supporting Information, Figure S14).

Heterogeneous nucleation of calcite on mica and gold in SFA is preceded by the nucleation of amorphous calcium carbonate. Although we directly observe the presence of ACC only in some of the experiments (slightly darker front appearing before the crystal growth in Supporting Information, Movies M03 and M06), the control experiments with argon purging, the aggregated nanoparticle character of the precipitates growing under the largest confinement (Figure S17), and more amorphous character of crystals in the presence of Mg^{2+}, which is known to stabilize ACC,[84] further indicate that the presence of ACC is characteristic for electrochemically induced calcite growth in our SFA pore. This is in line with multiple experiments detecting kinetically stabilized ACC under nano- to micron-scale confinement[9−18] and its subsequent transformation to crystalline $CaCO_3$ via heterogeneous nucleation.[18,21] As we previously discussed, the spatial confinement in our system can support a higher supersaturation with respect to calcium carbonate relative to an unconfined solution because of the generation of OH^- directly inside the pore. Based on pH modeling for an isolated gold surface (Supporting Information, Section S1), we estimated with PhreeqC that the lower bounds for the initial saturation indices under confinement are 1.95 for calcite, 0.47 for anhydrous ACC, and −0.49 for hydrated ACC (following thermodynamic data by Rodriguez-Navarro et al.[59]). As such, the initial solution confined in the SFA pore is likely supersaturated with respect to ACC. This is in line with our observations that calcite crystallizes only after the initial, likely very high, supersaturation which is partially lowered by the ACC precipitation.

In our experiments, the ACC front movement visualized in situ helps to track the evolution of supersaturation with respect to ACC within the SFA pore geometry. ACC front spreads simultaneously from two directions: from the disc edges (surface separations of a few 100 μm) toward the contact region and from the contact region (surface separations below 10 μm) toward the disc edges, indicating a complex development of supersaturation under the confinement of SFA (Supporting Information, Movie M03). As such, ACC nucleation around the contact edge within is faster than that in regions with intermediate surface separations (>10 μm). These supersaturation gradients develop due to reduced, diffusive transport under confinement. While the reduced transport under confinement would generally delay nucleation,[1,15,17] here, the effect is likely the opposite as the oxygen reduction reactions on the gold-confining wall elevate supersaturation with respect to $CaCO_3$ locally, inside the pore. The diffusive transport of OH^- from smaller toward larger surface separations is likely hindered, resulting in temporarily higher supersaturation with respect to the ACC around the contact region than at intermediate separations. Since we assume that in our experiments ACC nucleates homogeneously, we exclude that the high surface area of the confining walls or a specific pore geometry enhances nucleation within the contact region.[85] Thus, our measurements show that regulation of solution pH trapped within isolated compartments can facilitate crystallization in small nanoscale volumes, and it has been demonstrated that organisms can locally up-regulate pH during biomineralization.[86,87]

CONCLUSIONS

We synthesized calcite with hopper and tabular morphologies using the wedge-like confinement of the SFA. The precipitation was driven by an electrochemically assisted pH increase inside the pore formed by pressing mica and gold surfaces together. At surface separations above 5 μm, precipitation was limited to gold and yielded rhombohedral, (001)-oriented calcite bound by {104} planes. Larger calcite crystals exhibited hopper morphologies, representative of diffusion-instability-driven crystal growth. At gap thicknesses below 5 μm, the calcite precipitation was favored on the opposing mica surface and comprised flat calcite plates with rough (001) faces with thicknesses down to 40 nm. We attributed this preferential growth of the polar (001) faces of calcite on mica at the largest confinement to more favorable electrostatic interactions between mica and calcite nuclei than those between calcite and gold in the region of the overlapping electrical double layers of negatively charged mica and gold surfaces. Nanometer-thick calcite crystals, bound by planes typically absent on equilibrium crystal morphologies, could be synthesized without precipitation-modifying additives owing to the combination of confinement shape and inorganic confining wall materials that induce oriented crystal growth. Abundant and rapid crystal growth under nanoscale confinement could be achieved because of elevating the pH and thus the supersaturation with respect to calcium carbonate directly inside the pore. This strategy can be used to synthesize crystals with nontypical morphologies in a range of confined settings.

ASSOCIATED CONTENT

Data Availability Statement

All supporting movies and data used in this work can be openly accessed from the DataverseNO repository: 10.18710/LEKLRN.

Supporting Information

The Supporting Information is available free of charge at https://pubs.acs.org/doi/10.1021/acs.cgd.3c01433.

https://doi.org/10.1021/acs.cgd.3c01433
Cryst. Growth Des. XXXX, XXX, XXX−XXX

SFA setup information, SEM images, SFA data, AFM data, fluorescence data, epitaxy sketches, and analytical pH calculations on the isolated gold surface (PDF)

Supporting Movie M03 of calcite precipitation (MP4)

Supporting Movie M06 of calcite precipitation (MP4)

AUTHOR INFORMATION

Corresponding Author

Joanna Dziadkowiec − *The Njord Centre, Department of Physics, University of Oslo, Oslo 0371, Norway; Institute of Applied Physics, Applied Interface Physics, Vienna University of Technology, Vienna 1040, Austria;* orcid.org/0000-0001-6560-8744; Email: joanna.dziadkowiec@mn.uio.no

Authors

Gaute Linga − *PoreLab, The Njord Centre, Departments of Physics and Geosciences, University of Oslo, Oslo 0371, Norway*

Lukas Kalchgruber − *Institute of Applied Physics, Applied Interface Physics, Vienna University of Technology, Vienna 1040, Austria; CEST Centre for Electrochemical Surface Technology GmbH, Wiener Neustadt 2700, Austria*

Sunil Kavunga − *CEST Centre for Electrochemical Surface Technology GmbH, Wiener Neustadt 2700, Austria*

Hsiu-Wei Cheng − *Institute of Applied Physics, Applied Interface Physics, Vienna University of Technology, Vienna 1040, Austria;* orcid.org/0000-0001-8274-1707

Ola Nilsen − *Centre for Materials Science and Nanotechnology, Department of Chemistry, University of Oslo, Oslo 0315, Norway;* orcid.org/0000-0002-2824-9153

Coen Campsteijn − *Institute of Basic Medical Sciences, University of Oslo, Oslo 0317, Norway*

Boaz Pokroy − *Department of Materials Science and Engineering, Technion, Israel Institute of Technology, Haifa 32000, Israel;* orcid.org/0000-0003-0480-7250

Markus Valtiner − *Institute of Applied Physics, Applied Interface Physics, Vienna University of Technology, Vienna 1040, Austria; CEST Centre for Electrochemical Surface Technology GmbH, Wiener Neustadt 2700, Austria;* orcid.org/0000-0001-5410-1067

Complete contact information is available at: https://pubs.acs.org/10.1021/acs.cgd.3c01433

Notes

The authors declare no competing financial interest.

ACKNOWLEDGMENTS

This project received funding from the Research Council of Norway, FRIPRO grant nr 286733 (Solid−solid interfaces as critical regions in rocks and materials: probing forces, electrochemical reactions, friction, and reactivity). J.D. acknowledges funding from the Research Council of Norway, FRIPRO grant nr 344828, "Robert og Ella Wenzins legat" at the University of Oslo, and from "Elkem og Olge Adamsons stiftelse til støtte av geologisk forskning" foundation. G.L. acknowledges support from the Research Council of Norway, FRIPRO grant nr 325819. We thank the MIP Advanced Light Microscopy Core Facility at the Institute for Basic Medical Science (University of Oslo) for providing imaging facilities. We thank the anonymous Reviewers for valuable comments that helped to improve this work.

REFERENCES

(1) Meldrum, F. C.; O'Shaughnessy, C. Crystallization in confinement. *Adv. Mater.* **2020**, *32*, 2001068.

(2) Whittaker, M. L.; Dove, P. M.; Joester, D. Nucleation on surfaces and in confinement. *MRS Bull.* **2016**, *41*, 388−392.

(3) Gong, X.; Wang, Y.-W.; Ihli, J.; Kim, Y.-Y.; Li, S.; Walshaw, R.; Chen, L.; Meldrum, F. C. The crystal hotel: a microfluidic approach to biomimetic crystallization. *Adv. Mater.* **2015**, *27*, 7395−7400.

(4) Lertvachirapaiboon, C.; Pienpinijtham, P.; Wongravee, K.; Ekgasit, S. Optical properties of individual aragonite plates from nacre. *ChemistrySelect* **2018**, *3*, 11700−11704.

(5) Gower, L. B. Biomimetic model systems for investigating the amorphous precursor pathway and its role in biomineralization. *Chem. Rev.* **2008**, *108*, 4551−4627.

(6) Bjorkum, P.; Walderhaug, O. Geometrical arrangement of calcite cementation within shallow marine sandstones. *Earth-Sci. Rev.* **1990**, *29*, 145−161.

(7) Tegethoff, F. W.; Rohleder, J.; Kroker, E. *Calcium Carbonate: From the Cretaceous Period into the 21st Century*; Springer Science & Business Media, 2001.

(8) Gilbert, P. U.; Bergmann, K. D.; Boekelheide, N.; Tambutté, S.; Mass, T.; Marin, F.; Adkins, J. F.; Erez, J.; Gilbert, B.; Knutson, V.; et al. Biomineralization: Integrating mechanism and evolutionary history. *Sci. Adv.* **2022**, *8*, No. eabl9653.

(9) Page, K.; Stack, A. G.; Chen, S. A.; Wang, H.-W. Nanopore facilitated monohydrocalcitic amorphous calcium carbonate precipitation. *Phys. Chem. Chem. Phys.* **2022**, *24*, 18340−18346.

(10) Zeng, M.; Kim, Y.-Y.; Anduix-Canto, C.; Frontera, C.; Laundy, D.; Kapur, N.; Christenson, H. K.; Meldrum, F. C. Confinement generates single-crystal aragonite rods at room temperature. *Proc. Natl. Acad. Sci. U.S.A.* **2018**, *115*, 7670−7675.

(11) Stephens, C. J.; Ladden, S. F.; Meldrum, F. C.; Christenson, H. K. Amorphous calcium carbonate is stabilized in confinement. *Adv. Funct. Mater.* **2010**, *20*, 2108−2115.

(12) Dziadkowiec, J.; Zareeipolgardani, B.; Dysthe, D. K.; Røyne, A. Nucleation in confinement generates long-range repulsion between rough calcite surfaces. *Sci. Rep.* **2019**, *9*, 8948.

(13) Tester, C. C.; Wu, C.-H.; Weigand, S.; Joester, D. Precipitation of ACC in liposomes—a model for biomineralization in confined volumes. *Faraday Discuss.* **2012**, *159*, 345−356.

(14) Zeng, Y.; Cao, J.; Wang, Z.; Guo, J.; Lu, J. Formation of amorphous calcium carbonate and its transformation mechanism to crystalline CaCO3 in laminar microfluidics. *Cryst. Growth Des.* **2018**, *18*, 1710−1721.

(15) Wang, Y.; Zeng, M.; Meldrum, F. C.; Christenson, H. K. Using confinement to study the crystallization pathway of calcium carbonate. *Cryst. Growth Des.* **2017**, *17*, 6787−6792.

(16) Cavanaugh, J.; Whittaker, M. L.; Joester, D. Crystallization kinetics of amorphous calcium carbonate in confinement. *Chem. Sci.* **2019**, *10*, 5039−5043.

(17) Stephens, C. J.; Kim, Y.-Y.; Evans, S. D.; Meldrum, F. C.; Christenson, H. K. Early stages of crystallization of calcium carbonate revealed in picoliter droplets. *J. Am. Chem. Soc.* **2011**, *133*, 5210−5213.

(18) Wolf, S. E.; Leiterer, J.; Kappl, M.; Emmerling, F.; Tremel, W. Early homogenous amorphous precursor stages of calcium carbonate and subsequent crystal growth in levitated droplets. *J. Am. Chem. Soc.* **2008**, *130*, 12342−12347.

(19) Loste, E.; Park, R. J.; Warren, J.; Meldrum, F. C. Precipitation of calcium carbonate in confinement. *Adv. Funct. Mater.* **2004**, *14*, 1211−1220.

(20) Aizenberg, J.; Muller, D. A.; Grazul, J. L.; Hamann, D. Direct fabrication of large micropatterned single crystals. *Science* **2003**, *299*, 1205−1208.

(21) Katsman, A.; Polishchuk, I.; Pokroy, B. On the mechanism of calcium carbonate polymorph selection via confinement. *Faraday Discuss.* **2022**, *235*, 433−445.

(22) Livne, A.; Mijowska, S. C.; Polishchuk, I.; Mashikoane, W.; Katsman, A.; Pokroy, B. A fungal mycelium templates the growth of aragonite needles. *J. Mater. Chem. B* **2019**, *7*, 5725−5731.
(23) Schenk, A. S.; Albarracin, E. J.; Kim, Y.-Y.; Ihli, J.; Meldrum, F. C. Confinement stabilises single crystal vaterite rods. *Chem. Commun.* **2014**, *50*, 4729−4732.
(24) Volkmer, D.; Fricke, M.; Agena, C.; Mattay, J. Interfacial electrostatics guiding the crystallization of CaCO 3 underneath monolayers of calixarenes and resorcarenes. *J. Mater. Chem.* **2004**, *14*, 2249−2259.
(25) Kawano, J.; Shimobayashi, N.; Miyake, A.; Kitamura, M. Precipitation diagram of calcium carbonate polymorphs: its construction and significance. *J. Phys.: Condens. Matter* **2009**, *21*, 425102.
(26) Tribello, G. A.; Bruneval, F.; Liew, C.; Parrinello, M. A molecular dynamics study of the early stages of calcium carbonate growth. *J. Phys. Chem. B* **2009**, *113*, 11680−11687.
(27) Tester, C. C.; Whittaker, M. L.; Joester, D. Controlling nucleation in giant liposomes. *Chem. Commun.* **2014**, *50*, 5619−5622.
(28) Kashchiev, D.; Van Rosmalen, G. Review: Nucleation in solutions revisited. *Cryst. Res. Technol.* **2003**, *38*, 555−574.
(29) Aizenberg, J.; Black, A. J.; Whitesides, G. M. Oriented growth of calcite controlled by self-assembled monolayers of functionalized alkanethiols supported on gold and silver. *J. Am. Chem. Soc.* **1999**, *121*, 4500−4509.
(30) Hamilton, B. D.; Ha, J.-M.; Hillmyer, M. A.; Ward, M. D. Manipulating crystal growth and polymorphism by confinement in nanoscale crystallization chambers. *Acc. Chem. Res.* **2012**, *45*, 414−423.
(31) Yadlovker, D.; Berger, S. Nucleation and growth of single crystals with uniform crystallographic orientation inside alumina nanopores. *J. Appl. Phys.* **2007**, *101*, 101.
(32) Heywood, B. R.; Rajam, S.; Mann, S. Oriented crystallization of CaCO3 under compressed monolayers. Part 2.—Morphology, structure and growth of immature crystals. *J. Chem. Soc., Faraday Trans.* **1991**, *87*, 735−743.
(33) Xu, Y.; Nudelman, F.; Eren, E. D.; Wirix, M. J.; Cantaert, B.; Nijhuis, W. H.; Hermida-Merino, D.; Portale, G.; Bomans, P. H.; Ottmann, C.; et al. Intermolecular channels direct crystal orientation in mineralized collagen. *Nat. Commun.* **2020**, *11*, 5068.
(34) Hamilton, B. D.; Weissbuch, I.; Lahav, M.; Hillmyer, M. A.; Ward, M. D. Manipulating crystal orientation in nanoscale cylindrical pores by stereochemical inhibition. *J. Am. Chem. Soc.* **2009**, *131*, 2588−2596.
(35) Cantaert, B.; Beniash, E.; Meldrum, F. C. Nanoscale confinement controls the crystallization of calcium phosphate: relevance to bone formation. *Chem.—Eur. J.* **2013**, *19*, 14918−14924.
(36) Wu, H.; Cao, Y.; Ishige, R.; Higaki, Y.; Hoshino, T.; Ohta, N.; Takahara, A. Confinement-induced crystal growth in one-dimensional isotactic polystyrene nanorod arrays. *ACS Macro Lett.* **2013**, *2*, 414−418.
(37) Steinhart, M.; Göring, P.; Dernaika, H.; Prabhukaran, M.; Gösele, U.; Hempel, E.; Thurn-Albrecht, T. Coherent kinetic control over crystal orientation in macroscopic ensembles of polymer nanorods and nanotubes. *Phys. Rev. Lett.* **2006**, *97*, 027801.
(38) Li, L.; Kohler, F.; Røyne, A.; Dysthe, D. K. Growth of calcite in confinement. *Crystals* **2017**, *7*, 361.
(39) Kohler, F.; Pierre-Louis, O.; Dysthe, D. K. Crystal growth in confinement. *Nat. Commun.* **2022**, *13*, 6990.
(40) Bresme, F.; Cámara, L. G. Computer simulation studies of crystallization under confinement conditions. *Chem. Geol.* **2006**, *230*, 197−206.
(41) Hedges, L. O.; Whitelam, S. Patterning a surface so as to speed nucleation from solution. *Soft Matter* **2012**, *8*, 8624−8635.
(42) Gabrielli, C.; Maurin, G.; Poindessous, G.; Rosset, R. Nucleation and growth of calcium carbonate by an electrochemical scaling process. *J. Cryst. Growth* **1999**, *200*, 236−250.
(43) Haaring, R.; Kumar, N.; Bosma, D.; Poltorak, L.; Sudhölter, E. J. R. Electrochemically Assisted deposition of calcite for application in surfactant adsorption studies. *Energy Fuels* **2019**, *33*, 805−813.
(44) Tlili, M.; Benamor, M.; Gabrielli, C.; Perrot, H.; Tribollet, B. Influence of the Interfacial pH on Electrochemical CaCO[sub 3] Precipitation. *J. Electrochem. Soc.* **2003**, *150*, C765.
(45) Valtiner, M.; Banquy, X.; Kristiansen, K.; Greene, G. W.; Israelachvili, J. N. The electrochemical surface forces apparatus: The effect of surface roughness, electrostatic surface potentials, and anodic oxide growth on interaction forces, and friction between dissimilar surfaces in aqueous solutions. *Langmuir* **2012**, *28*, 13080−13093.
(46) Grünewald, T.; Dähne, L.; Helm, C. A. Supersaturation and crystal nucleation in confined geometries. *J. Phys. Chem. B* **1998**, *102*, 4988−4993.
(47) Akbulut, M.; Chen, N.; Maeda, N.; Israelachvili, J.; Grunewald, T.; Helm, C. A. Crystallization in thin liquid films induced by shear. *J. Phys. Chem. B* **2005**, *109*, 12509−12514.
(48) Liberto, T.; Nenning, A.; Bellotto, M.; Dalconi, M. C.; Dworschak, D.; Kalchgruber, L.; Robisson, A.; Valtiner, M.; Dziadkowiec, J. Detecting Early-Stage Cohesion Due to Calcium Silicate Hydration with Rheology and Surface Force Apparatus. *Langmuir* **2022**, *38*, 14988−15000.
(49) Dziadkowiec, J.; Røyne, A. Nanoscale Forces between Basal Mica Surfaces in Dicarboxylic Acid Solutions: Implications for Clay Aggregation in the Presence of Soluble Organic Acids. *Langmuir* **2020**, *36*, 14978−14990.
(50) Hegner, M.; Wagner, P.; Semenza, G. Ultralarge atomically flat template-stripped Au surfaces for scanning probe microscopy. *Surf. Sci.* **1993**, *291*, 39−46.
(51) Wieser, V.; Bilotto, P.; Ramach, U.; Yuan, H.; Schwenzfeier, K.; Cheng, H.-W.; Valtiner, M. Novel in situ sensing surface forces apparatus for measuring gold versus gold, hydrophobic, and biophysical interactions. *J. Vac. Sci. Technol., A* **2021**, *39*, 023201.
(52) Israelachvili, J.; Min, Y.; Akbulut, M.; Alig, A.; Carver, G.; Greene, W.; Kristiansen, K.; Meyer, E.; Pesika, N.; Rosenberg, K.; et al. Recent advances in the surface forces apparatus (SFA) technique. *Rep. Prog. Phys.* **2010**, *73*, 036601.
(53) Dziadkowiec, J.; Javadi, S.; Bratvold, J. E.; Nilsen, O.; Røyne, A. Surface Forces Apparatus measurements of interactions between rough and reactive calcite surfaces. *Langmuir* **2018**, *34*, 7248−7263.
(54) Maslova, M.; Gerasimova, L.; Forsling, W. Surface properties of cleaved mica. *Colloid J.* **2004**, *66*, 322−328.
(55) Rathod, B. B.; Murthy, S.; Bandyopadhyay, S. Is this solution pink enough? a smartphone tutor to resolve the eternal question in phenolphthalein-based titration. *J. Chem. Educ.* **2019**, *96*, 486−494.
(56) Molnár, Z.; Dódony, I.; Pósfai, M. Transformation of amorphous calcium carbonate in the presence of magnesium, phosphate, and mineral surfaces. *Geochim. Cosmochim. Acta* **2023**, *345*, 90−101.
(57) Zehner, J.; Røyne, A.; Wentzel, A.; Sikorski, P. Microbial-induced calcium carbonate precipitation: an experimental toolbox for in situ and real time investigation of micro-scale pH evolution. *RSC Adv.* **2020**, *10*, 20485−20493.
(58) Parkhurst, D. L.; Appelo, C.; et al. User's guide to PHREEQC (Version 2): A computer program for speciation, batch-reaction, one-dimensional transport, and inverse geochemical calculations. *Water-resources investigations report* 1999; Vol *99*, p 312.
(59) Rodriguez-Navarro, C.; Kudłacz, K.; Cizer, O.·.; Ruiz-Agudo, E. Formation of amorphous calcium carbonate and its transformation into mesostructured calcite. *CrystEngComm* **2015**, *17*, 58−72.
(60) Yang, Z.; Zhang, J.; Zhang, L.; Fu, B.; Tao, P.; Song, C.; Shang, W.; Deng, T. Self-Assembly in Hopper-Shaped Crystals. *Adv. Funct. Mater.* **2020**, *30*, 1908108.
(61) Mullins, W. W.; Sekerka, R. F. Morphological stability of a particle growing by diffusion or heat flow. *J. Appl. Phys.* **1963**, *34*, 323−329.
(62) Chernov, A. Stability of faceted shapes. *J. Cryst. Growth* **1974**, *24*−*25*, 11−31.

https://doi.org/10.1021/acs.cgd.3c01433
Cryst. Growth Des. XXXX, XXX, XXX−XXX

(63) Desarnaud, J.; Derluyn, H.; Carmeliet, J.; Bonn, D.; Shahidzadeh, N. Hopper growth of salt crystals. *J. Phys. Chem. Lett.* **2018**, *9*, 2961−2966.
(64) Sunagawa, I. Characteristics of crystal growth in nature as seen from the morphology of mineral crystals. *Bulletin de minéralogie* **1981**, *104*, 81−87.
(65) Gabrielli, C.; Jaouhari, R.; Joiret, S.; Maurin, G.; Rousseau, P. Study of the electrochemical deposition of CaCO3 by in situ Raman spectroscopy: I. Influence of the substrate. *J. Electrochem. Soc.* **2003**, *150*, C478.
(66) Granit, N. F.; Korin, E.; Bettelheim, A. Effect of organic additives on electrochemical surface precipitation and polymorphism of CaCO3. *Chem. Eng. Technol.* **2003**, *26*, 341−346.
(67) Tlili, M. M.; Amor, M. B.; Gabrielli, C.; Joiret, S.; Maurin, G.; Rousseau, P. Study of electrochemical deposition of CaCO3 by in situ raman spectroscopy: II. Influence of the solution composition. *J. Electrochem. Soc.* **2003**, *150*, C485.
(68) Teghidet, H.; Bernard, M. C.; Borensztajn, S.; Chaal, L.; Joiret, S.; Saidani, B. Calcite epitaxy on Au and Ag (1 1 1). *J. Cryst. Growth* **2011**, *331*, 72−77.
(69) Stephens, C. J.; Mouhamad, Y.; Meldrum, F. C.; Christenson, H. K. Epitaxy of calcite on mica. *Cryst. Growth Des.* **2010**, *10*, 734−738.
(70) Brugman, S. J.; Ottenbros, A. B.; Megens, F.; van Enckevort, W. J.; Vlieg, E. Epitaxy of Rhodochrosite (MnCO3) on Muscovite Mica and Its Relation with Calcite (CaCO3). *Cryst. Growth Des.* **2020**, *20*, 4802−4810.
(71) Xu, X.-R.; Pan, H.-H.; Tang, R.-K.; Cho, K. Additive-dependent morphogenesis of oriented calcite crystals on mica. *CrystEngComm* **2011**, *13*, 6311−6314.
(72) Pokroy, B.; Kapon, M.; Marin, F.; Adir, N.; Zolotoyabko, E. Protein-induced, previously unidentified twin form of calcite. *Proc. Natl. Acad. Sci. U.S.A.* **2007**, *104*, 7337−7341.
(73) Franceschi, G.; Kocán, P.; Conti, A.; Brandstetter, S.; Balajka, J.; Sokolović, I.; Valtiner, M.; Mittendorfer, F.; Schmid, M.; Setvín, M.; et al. Resolving the intrinsic short-range ordering of K+ ions on cleaved muscovite mica. *Nat. Commun.* **2023**, *14*, 208.
(74) Jurca, H.; Damian, A.; Gougaud, C.; Thiaudière, D.; Cortès, R.; Maroun, F.; Allongue, P. Epitaxial electrodeposition of Fe on Au (111): structure, nucleation, and growth mechanisms. *J. Phys. Chem. C* **2016**, *120*, 16080−16089.
(75) Wang, J.; Davenport, A. J.; Isaacs, H. S.; Ocko, B. Surface charge—Induced ordering of the Au (111) surface. *Science* **1992**, *255*, 1416−1418.
(76) Rojas, O. J.; Claesson, P. M.; Muller, D.; Neuman, R. D. The effect of salt concentration on adsorption of low-charge-density polyelectrolytes and interactions between polyelectrolyte-coated surfaces. *J. Colloid Interface Sci.* **1998**, *205*, 77−88.
(77) Wang, J.; Bard, A. J. Direct atomic force microscopic determination of surface charge at the gold/electrolyte interface the inadequacy of classical GCS theory in describing the double-layer charge distribution. *J. Phys. Chem. B* **2001**, *105*, 5217−5222.
(78) Bruno, M.; Massaro, F. R.; Prencipe, M.; Aquilano, D. Surface reconstructions and relaxation effects in a centre-symmetrical crystal: the {00.1} form of calcite (CaCO 3). *CrystEngComm* **2010**, *12*, 3626−3633.
(79) Gu, D.; Yalcin, S.; Baumgart, H.; Qian, S.; Baysal, O.; Beskok, A. Electrophoretic light scattering for surface zeta potential measurement of ALD metal oxide films. *ECS Trans.* **2010**, *33*, 37−41.
(80) Xia, Z.; Rozyyev, V.; Mane, A. U.; Elam, J. W.; Darling, S. B. Surface zeta potential of ALD-grown metal-oxide films. *Langmuir* **2021**, *37*, 11618−11624.
(81) Rajam, S.; Mann, S. Selective stabilization of the (001) face of calcite in the presence of lithium. *J. Chem. Soc., Chem. Commun.* **1990**, 1789−1791.
(82) Matijaković Mlinarić, N.; Kontrec, J.; Njegić Džakula, B.; Falini, G.; Kralj, D. Role of hydrodynamics, li+ addition and transformation kinetics on the formation of plate-like {001} calcite crystals. *Crystals* **2021**, *11*, 250.
(83) Wang, T.; Antonietti, M.; Cölfen, H. Calcite mesocrystals:"-Morphing" crystals by a polyelectrolyte. *Chem.—Eur. J.* **2006**, *12*, 5722−5730.
(84) Loste, E.; Wilson, R. M.; Seshadri, R.; Meldrum, F. C. The role of magnesium in stabilising amorphous calcium carbonate and controlling calcite morphologies. *J. Cryst. Growth* **2003**, *254*, 206−218.
(85) Page, A. J.; Sear, R. P. Crystallization controlled by the geometry of a surface. *J. Am. Chem. Soc.* **2009**, *131*, 17550−17551.
(86) Wall, M.; Ragazzola, F.; Foster, L. C.; Form, A.; Schmidt, D. N. pH up-regulation as a potential mechanism for the cold-water coral <i>Lophelia pertusa</i> to sustain growth in aragonite undersaturated conditions. *Biogeosciences* **2015**, *12*, 6869−6880.
(87) Hu, M. Y.; Yan, J.-J.; Petersen, I.; Himmerkus, N.; Bleich, M.; Stumpp, M. A SLC4 family bicarbonate transporter is critical for intracellular pH regulation and biomineralization in sea urchin embryos. *eLife* **2018**, *7*, No. e36600.

https://doi.org/10.1021/acs.cgd.3c01433
Cryst. Growth Des. XXXX, XXX, XXX−XXX